Article

Not peer-reviewed version

Low-Frequency, Pulsatile Delivery of Water Vapor to the Maxillary Sinus: Feasibility, Limitations, and Design Implications

Amr Seifelnasr , Xiuhua Si , Jinxiang Xi *

Posted Date: 1 June 2026

doi: 10.20944/preprints202606.0021.v1

Keywords: maxillary sinus; paranasal sinuses; pulsatile aerosol delivery; intranasal drug delivery; water aerosol; aerosol deposition; chronic rhinosinusitis doi:10.20944/preprints202606.0021.v1

Article

Low-Frequency, Pulsatile Delivery of Water Vapor to the Maxillary Sinus: Feasibility, Limitations, and Design Implications

Amr Seifelnasr [1], Xiuhua Si [2] and Jinxiang Xi [1,*]

[1] Department of Biomedical Engineering, University of Massachusetts, Lowell, MA 01854, USA
[2] Department of Aerospace, Industrial, and Mechanical Engineering, California Baptist University, Riverside, CA 92504, USA
* Correspondence: jinxiang_xi@uml.edu; Tel.: 1-978-934-3259

Abstract

Efficient aerosol delivery to the maxillary sinuses remains challenging because narrow ostia limit sinus entry. This in vitro study evaluated whether low-frequency, large-amplitude pulsatile flow can deliver humidifier-generated water aerosols to the maxillary sinuses, compared retention with e-vapor under identical conditions, and identified setup modifications required for water aerosol transport. Experiments used three transparent anatomically realistic sinonasal models: two single-passage models with narrow-long (NL) and wide-short (WS) ostial geometries, and one dual-passage dual-maxillary-sinus model (RL). Water aerosols and e-vapor were delivered using a modified servo-actuated syringe generator under fixed conditions: 50 mL stroke volume, 0.33 Hz frequency, 1 L/min vacuum-induced flow, and 1.5 min delivery. Water aerosols were larger than e-vapor aerosols (D50 = 5.553 µm vs. 3.394 µm) and required setup modification because of greater wall interactions, condensation, coalescence, and transport losses. Pulsatile delivery achieved plume entry into all tested maxillary sinuses. E-vapor showed greater retained mass than water aerosols in NL (1.060 ± 0.152 vs. 0.540 ± 0.089 mg) and WS (0.800 ± 0.071 vs. 0.520 ± 0.110 mg). Water-sensitive Sar-Gel visualization confirmed bilateral water aerosol retention in RL. These findings support pulsatile delivery as a feasible strategy for water aerosol transport to the maxillary sinuses, but with a lower efficiency than e-vapor aerosols.

Keywords: maxillary sinus; paranasal sinuses; pulsatile aerosol delivery; intranasal drug delivery; water aerosol; aerosol deposition; chronic rhinosinusitis

1. Introduction

Chronic rhinosinusitis (CRS) is a common inflammatory disorder of the sinonasal mucosa that is associated with considerable symptom burden, impaired quality of life, and substantial healthcare utilization [1–3]. Because CRS involves inflammation of sinonasal tissues, topical intranasal therapy remains an important treatment approach by enabling localized drug administration while limiting systemic exposure [4–8]. However, the effectiveness of topical therapy depends not only on the administered formulation, but also on delivery-device and fluid-dynamic factors that determine whether a sufficient fraction of the dose reaches the intended sinonasal target region [8,9]. Delivery to the paranasal sinuses remains particularly challenging because the sinus cavities communicate with the nasal airway through relatively narrow ostial openings that restrict airflow exchange and particle transport [10–13].

Conventional intranasal delivery approaches face important transport limitations before the administered formulation reaches the sinus ostia. Nasal spray dosimetry depends strongly on spray characteristics and administration conditions, including droplet size, plume geometry, and spray angle [14,15]. The nasal anatomy, including localized constrictions near the nasal valve and rapid changes in airflow direction within the vestibular region, can promote anterior or non-target deposition before particles reach posterior sinonasal targets such as the middle meatus and sinus ostia [14–16]. These upstream transport losses are further influenced by patient-specific nasal geometry and delivery technique, contributing to the limited and variable sinus delivery commonly observed with standard nasal sprays and nebulized aerosol delivery systems [6,9,17,18].

Even when aerosols reach the sinus ostial opening, entry into the sinus lumen remains restricted by limited sinus ventilation and resistance to airflow exchange through the ostial pathway. Sinus aerosol delivery and ventilation studies demonstrate that restricted ostial exchange is a major barrier to aerosol penetration into the paranasal sinuses [19–21]. Anatomical and computational studies further show that maxillary sinus ventilation and topical drug delivery are strongly affected by ostial geometry and by anatomical changes that alter sinus access, such as surgically enlarged ostial pathways [13,22,23]. Post-operative studies also demonstrate that endoscopic sinus surgery can alter nasal spray deposition patterns within the sinonasal cavity [24].

To overcome these anatomical and transport barriers, several studies have investigated delivery approaches that impose oscillatory, acoustic, or pulsatile flow disturbances to enhance aerosol access to the paranasal sinuses. Acoustic airflow, sonic aerosol delivery, and pulsatile aerosol systems have been reported to improve sinus drug delivery by generating time-varying pressure and airflow disturbances across the sinus ostia [19–21,25–33]. Related ventilation studies, including humming-induced sinus gas-exchange studies and recent in vitro studies of pulsatile flow and structural vibration, further support the concept that oscillatory pressure or flow disturbances can enhance exchange across the ostial pathway [34–37]. Together, these studies support the use of time-varying flow or pressure disturbances as a strategy to improve aerosol access to sinus cavities where natural ventilation and ostial exchange are limited.

Despite these advances, efficient and reproducible aerosol delivery to the paranasal sinuses remains difficult. Reported sinus deposition efficiencies often remain low relative to the emitted dose, and delivery outcomes remain strongly influenced by anatomy, delivery conditions, aerosol properties, and device configuration [8,9,14,15,21,32]. Moreover, although prior pulsatile and acoustic studies have demonstrated enhanced sinus transport, the translation of pulsatile delivery approaches across aerosol formulations with different physicochemical properties remains insufficiently understood. A recent study from our group demonstrated that low-frequency, large-amplitude pulsatile actuation enhanced e-vapor transport into the maxillary sinuses of anatomically realistic sinonasal models, with retained aerosol mass varying according to delivery conditions and ostial geometry [21]. That study showed that maxillary sinus delivery was governed by both controllable delivery conditions, including pulsation amplitude, pulsation frequency, and imposed nasal airflow, and anatomical factors such as ostial geometry. These findings supported the role of transient pressure-driven exchange in improving aerosol access to the maxillary sinus. Although e-vapor provided a useful medium for visualizing pulsatile aerosol transport and may also serve as a potential carrier platform, many therapeutic intranasal products are conventionally formulated as aqueous solutions or suspensions [38–40]. Accordingly, evaluating whether this pulsatile delivery approach can be adapted from oil-based e-vapor aerosols to water-based aerosols as drug carriers represents an important step toward assessing its relevance for clinically applicable sinonasal drug delivery systems.

This translation is not straightforward because aerosol formulation and liquid-phase behavior can substantially influence aerosol transport, wall interactions, condensation/evaporation dynamics, coalescence, and deposition patterns [41–44]. In preliminary testing using the initial e-vapor delivery setup [21], humidifier-generated water aerosols exhibited stronger surface interactions and greater susceptibility to condensation, coalescence, and transport losses within the delivery pathway compared with e-vapor aerosols. These formulation-dependent differences suggested that a pulsatile delivery architecture developed using e-vapor aerosols could not be directly transferred to water-based aerosol delivery without modification. Therefore, the objective of this study was to evaluate the feasibility of delivering water-based aerosols to the maxillary sinuses using low-frequency, large-amplitude pulsatile flow and to identify the key modifications required to adapt the initial e-vapor-based delivery approach for water aerosol transport. This study further aimed to generate quantitative and qualitative data to inform the design and development of pulsatile intranasal delivery systems for water-based aerosol delivery to the paranasal sinuses. Specific aims included:

1. Evaluate the feasibility of transporting water aerosols into the maxillary sinuses using low-frequency, large-amplitude pulsatile flow.
2. Compare the transport and retention behavior of water aerosols and e-vapor within anatomically realistic sinonasal models, under identical delivery conditions.
3. Assess the influence of sinonasal geometry and administration nostril on aerosol transport and retained dose.

2. Materials and Methods

2.1. Study Design

A controlled in vitro study was conducted to evaluate the feasibility of delivering water aerosols to the maxillary sinuses using low-frequency, large-amplitude pulsatile flows. The present investigation builds on an initial e-vapor pulsatile delivery study from our group [21], in which successful delivery of e-vapor into the maxillary sinuses was demonstrated using anatomically realistic sinonasal models under externally generated pulsatile flow conditions. Two aerosol media were investigated in the present study: (1) humidifier-generated water aerosols produced using an ultrasonic cool-mist humidifier (Model AO-101, AquaOasis, USA) with a 2.2 L water tank, and (2) oil-based e-vapor aerosols generated using a fog machine (LENSGO, Shenzhen, Guangdong, China) from a formulation comprising 30% v/v propylene glycol and 70% v/v vegetable glycerin. Preliminary testing demonstrated that the experimental setup previously used for e-vapor delivery [21] was not directly suitable for water aerosol transport because water aerosols exhibited substantially greater aerosol losses and flow obstruction within portions of the delivery system. Accordingly, modifications to the pulsatile delivery setup were implemented in the present study to accommodate the differing transport characteristics of water vapor aerosols.

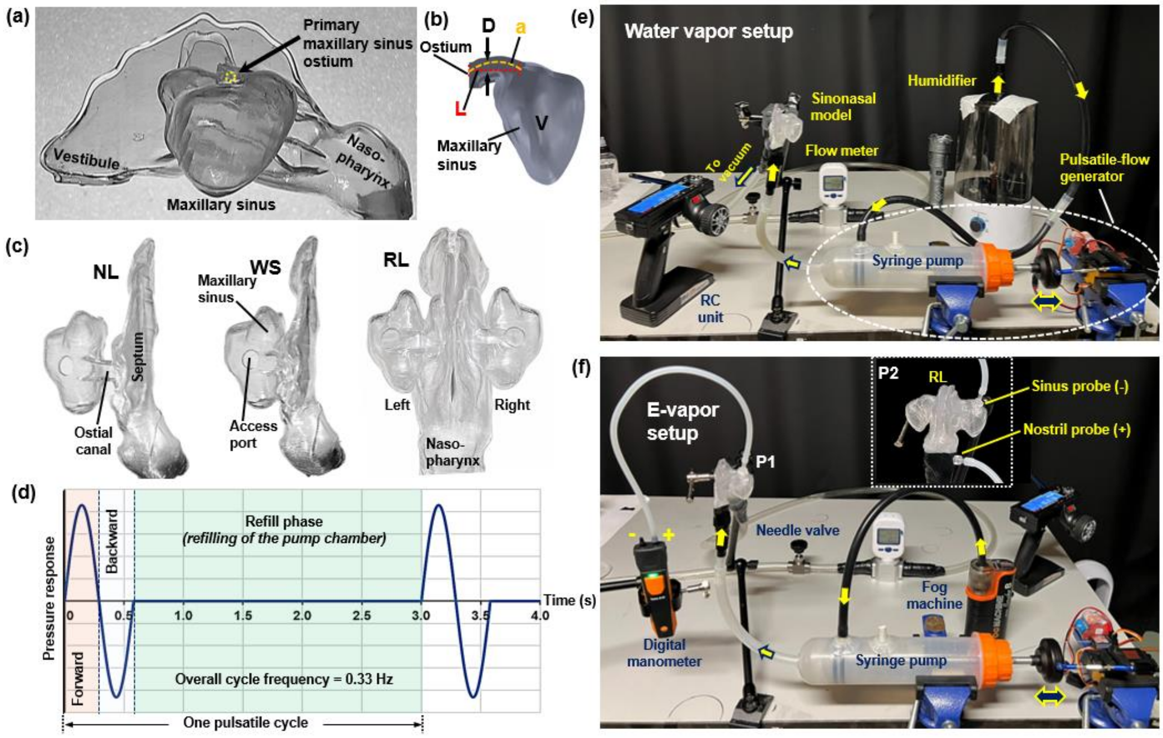

Figure 1. Sinonasal casts and experimental setup. (a) Transparent single-passage sinonasal model showing key anatomical regions. (b) Coronal view of the ostial canal and maxillary sinus indicating geometrical parameters (ostial canal width, D; ostial canal length, L; and sinus cavity volume, V). (c) Top views of the three sinonasal models: the narrow-long ostial canal model (NL), the wide-short ostial canal model (WS), and the dual-passage dual-maxillary-sinus model (RL). The access ports located on the roof of the maxillary sinuses are indicated; these were used for both pressure measurements and mass-deposition quantification via cotton swab sampling. (d) Schematic representation of one intermittent pulsatile actuation cycle used for aerosol delivery, illustrating the forward stroke, backward stroke, and refill phase required for replenishment of the pump chamber with aerosols between successive pulses. (e) Experimental setup for pulsatile delivery of water vapor generated by a humidifier. (f) Experimental setup for pulsatile delivery of oil-based e-vapor generated by a fog machine. Also shown are the digital manometer configurations used for probing gauge pressure within the sinus lumen (P1) and differential pressure between the nostril inlet and sinus lumen (P2).

Pulsatile delivery was generated using a custom-built servo-actuated syringe-based pulsation generator (Table 1). The reciprocating syringe piston generated a stroke volume (SV) of 50 mL during each cycle (Figure 1d). Additional delivery conditions included a pulsatile frequency (f) of 0.33 Hz, vacuum-induced nasopharyngeal flow rate (Q) of 1 L/min, and delivery duration of 1.5 min. During each pulsatile actuation cycle, the piston underwent a forward stroke followed by a backward stroke, after which a refill phase was required to allow replenishment of the pump chamber with aerosols prior to the subsequent actuation (Figure 1d). The intermittent refill phase was necessary because preliminary testing demonstrated that the humidifier-generated water aerosols could not replenish the chamber rapidly enough for continuous high-frequency cyclic operation. The same intermittent pulsatile waveform was also used for e-vapor delivery experiments to maintain consistent operating conditions for comparison purposes.

The primary outcomes assessed in the present study included sinonasal pressure measurements, spatiotemporal plume propagation behavior, retained aerosol mass (M_{ret}), and qualitative visualization of retained water aerosol deposition using Sar-Gel.

Table 1. Geometrical characteristics of the sinonasal models, ostial canal dimensions, sinus cavity volumes, and pulsatile delivery conditions.

Sinonasal model	Min. CSA* (mm^2)	Hydraulic diameter, D (mm)	Ostial canal chord length, L (mm)	Ostial canal arc length, a (mm)	Tortuosity, a/L	Maxillary sinus volume, V (mL)
NL	**11.05**	**3.20**	**10.73**	**11.02**	**1.03**	**13.408**
WS	**21.38**	**4.40**	**3.56**	**4.30**	**1.21**	**13.408**
RL-Right sinus	**13.41**	**3.67**	**5.76**	**6.86**	**1.19**	**10.284**
RL-Left sinus	**11.48**	**3.29**	**5.27**	**6.23**	**1.18**	**10.302**
Delivery conditions					**Value**	
SV (mL)					**50**	
f (Hz)					**0.33**	
Q (L/min)					**1**	
Servo dV/dt (mL/s)					**172.41**	
Delivery duration (min)					**1.5**	

*CSA: Cross-sectional area.

2.2. Sinonasal Models

Three transparent anatomically realistic *in vitro* sinonasal models featuring only the maxillary sinuses were used (Figures 1a-c; Table 1): a narrow-long ostial canal single-passage model (NL), a wide-short ostial canal single-passage model (WS), and a dual-passage dual-maxillary-sinus model (RL). The NL and WS models differed solely in ostial canal geometry (Figure 1b), namely the

doi:10.20944/preprints202606.0021.v1

hydraulic diameter (D) corresponding to the location of the minimum cross-sectional area (CSA), ostial canal chord length (L), ostial canal arc length (a), and tortuosity (a/L), while maintaining a constant maxillary sinus cavity volume (V) (Table 1). These modifications were implemented to generate controlled sinonasal variants featuring a constricted maxillary ostial canal (NL) and a substantially more patent ostial geometry (WS).

The RL model retained both the right and left maxillary sinuses (Figure 1c, third panel). Unlike the NL and WS variants, which incorporated controlled geometrical modifications, the RL model preserved the original MRI-derived maxillary sinus ostia and maxillary sinus cavity volumes, including differences between the right and left maxillary sinuses (Table 1). The ostial geometrical dimensions and maxillary sinus cavity volumes, whether modified or maintained from the original MRI geometry, fell within reported anatomical ranges [10,45–48]. The casts were fabricated using a stereolithography 3D printer (Stratasys Neo450s, Stratasys, Eden Prairie, MN, USA) with a 2-mm wall thickness from a transparent resin material (Somos WaterShed XC 11122, Stratasys, Eden Prairie, MN, USA).

2.3. Experimental Setup

2.3.1. Original Setup Limitations

The pulsatile delivery architecture used in the present investigation was adapted from an initial e-vapor-based setup developed for low-frequency, large-amplitude pulsatile delivery of e-vapor aerosols to the maxillary sinuses [21]. The initial configuration incorporated one-way check valves to establish the transient pulsatile pressure disturbances required for aerosol entry into the sinus cavity and demonstrated successful e-vapor delivery under externally imposed pulsatile flow conditions [21]. Preliminary testing demonstrated that direct implementation of the prior setup for humidifier-generated water aerosols resulted in substantially diminished aerosol transport performance, consistent with Nagel et al who observed that valve geometry significantly altered aerosol delivery behavior [49]. Compared with e-vapor aerosols, water aerosols exhibited greater wall affinity and condensation tendencies within the delivery pathway, resulting in coalescence and formation of larger droplets [50–52]. These effects promoted inertial impaction and accumulation within the one-way valve assemblies, progressively restricting aerosol transport and reducing aerosol concentration delivered to the administration outlet. Under extended operation, progressive accumulation within the valve body occasionally resulted in severe transport restriction or complete cessation of aerosol passage.

Removal of the one-way valves in attempts to alleviate transport restriction proved ineffective because elimination of the valves substantially reduced the transient pulsatile pressure disturbances necessary to facilitate effective sinus entry. Accordingly, revision of the original setup architecture was required to accommodate the differing transport characteristics of water aerosols while preserving the ability of the system to generate transient pressure conditions sufficient to promote sinus delivery. The principal modifications implemented relative to the initial e-vapor-based setup are summarized in Table 2.

Table 2. Main modifications in the pulsatile delivery setup relative to the initial delivery system [21].

Feature	Initial setup	Modified setup (Present study)	Rationale
Aerosol medium	**E-vapor only**	**Water aerosols and e-vapor**	**Extend technique to water aerosol delivery**
Downstream one-way valves	**Present**	**Eliminated**	**Water aerosols promoted coalescence, condensation, and transport restriction**

Chamber filling mechanism	**Valve-based architecture**	**Syringe intake port allowing filling during backstroke**	**Enable efficient chamber replenishment**
Chamber refill strategy	**Continuous cyclic operation**	**Intermittent refill phase introduced**	**Humidifier aerosol output required additional time for complete chamber replenishment between pulsatile actuation cycles**
Pulsatile waveform	**Continuous pulsatile cycling**	**Forward stroke + backward stroke + refill phase**	**Accommodate intermittent operation required for water aerosol delivery**
Setup compatibility	**Optimized for e-vapor**	**Modified for water aerosols while maintaining e-vapor compatibility**	**Enable formulation comparison**

2.3.2. Modified Pulsatile Delivery Setup

The modified pulsatile delivery setup employed in the present study utilized a custom-built servo-actuated syringe-based pulsation generator configured to generate intermittent large-amplitude pulsatile flow disturbances (Figures 1d-f). The system architecture eliminated the downstream one-way valve configuration used in the initial e-vapor-based setup [21] and instead incorporated an aerosol intake port within the syringe body to permit chamber filling during piston retraction. The pulsation generator comprised a 500 mL extraction and fill syringe pump (HORUSDY, Hangzhou, China) modified to contain a 10 mm inner diameter aerosol intake port within the syringe body. The intake port incorporated an inlet nozzle providing an airtight connection to a 10 mm inner diameter silicone tube that supplied aerosols from either a humidifier (Model AO-101; AquaOasis, USA) (Figure 1e) or a fog machine (LENSGO, Shenzhen, Guangdong, China) (Figure 1f), depending on the aerosol medium under investigation. The experimental setup shown in Figures 1e and 1f differed only in the aerosol generation source, whereas all remaining delivery system components and operating conditions were kept identical. A piston stopper limited the effective chamber displacement volume to 50 mL, which was taken as the stroke volume (SV) used throughout the study.

The syringe handle was mechanically coupled through a turnbuckle rod to a rotary servomotor (JX PDI-HV2060MG, Shantou JiXian Electronic Technology Co., Ltd., Guangdong, China). Servo operation was controlled using a 2.4 GHz radio control system (Flysky GT3B, Shenzhen Flysky Technology Co., Ltd., Shenzhen, China). The servomotor was programmed to actuate the piston over a fixed travel distance corresponding to a forward stroke volume of 50 mL followed by a backward stroke volume of 50 mL during each pulsatile actuation cycle. A 30 cm length of silicone tubing (10 mm inner diameter) connected the syringe output to the administration nostril of the sinonasal model. The maxillary sinus access ports located on the roof of the sinus cavities (Figure 1c) were sealed using transparent waterproof polyurethane film dressing tape (G18334, Fukaisu, China) during delivery experiments to maintain a closed system during pulsatile aerosol administration and pressure measurements. A laboratory vacuum source was used to establish the imposed inhalation flow condition (Q). For the single-passage NL and WS models, suction was applied at the nasopharyngeal outlet. For the RL model, suction was applied through the nostril contralateral to the nostril of aerosol administration while the nasopharyngeal outlet was sealed. A flow meter (MF5706, Siargo Ltd., Santa Clara, CA, USA) and needle valve were connected in line with the vacuum source to regulate and maintain the prescribed inhalation flow condition. During the backward stroke, aerosols entered the syringe chamber through the intake port to replenish the chamber volume. During the subsequent forward stroke, piston advancement sealed the intake opening, creating a fully enclosed chamber volume that compressed and discharged aerosols through the administration outlet under transient positive pressure conditions.

Preprints.org (www.preprints.org) | NOT PEER-REVIEWED | Posted: 1 June 2026 doi:10.20944/preprints202606.0021.v1

The pulsatile delivery technique employed intermittent large-amplitude pulsations generated through reciprocating piston actuation. During each actuation cycle, the piston underwent a forward stroke followed by a backward stroke, after which a refill phase was required to allow replenishment of the pump chamber before subsequent actuation. Preliminary testing demonstrated that humidifier-generated water aerosols could not replenish the chamber sufficiently rapidly for continuous high-frequency cyclic operation while maintaining adequate aerosol concentration. Accordingly, intermittent operation was implemented consisting of a transient forward/backward actuation event followed by a refill interval, resulting in an overall cycle frequency of approximately 0.33 Hz (Figure 1d). The intermittent pulsatile waveform may be represented schematically as:

$$P(t) = \begin{cases} P_{max}\sin\left(\frac{2\pi t}{0.58}\right), & 0 \le t < 0.58\ s \\ 0, & 0.58 \le t < 3.0\ s \end{cases} \tag{1}$$

where the active phase represents the combined forward and backward piston strokes and the remaining interval represents replenishment of the pump chamber before the subsequent cycle. The waveform is conceptual and intended to illustrate the intermittent operating principle rather than a measured transient pressure profile. The same intermittent pulsatile waveform was also applied during e-vapor experiments to maintain consistent operating conditions between aerosol media.

2.4. Aerosol Characterization

Particle size distributions of the generated aerosols were characterized using a laser diffraction particle size analyzer (Spraylink, Dickinson, TX, USA). Representative plume visualizations were generated for both water aerosols and e-vapor using the same 10 mm inner-diameter silicone outlet tube connected to either the humidifier or fog machine output, depending on the aerosol medium under investigation. Plume visualization images were captured using an iPhone 13 Pro camera (Apple Inc., Cupertino, CA, USA) operating at 240 frames per second.

2.5. Pressure Measurements

Sinonasal pressure measurements were performed using a digital differential pressure manometer (Testo 510i Smart Probe, Testo SE & Co. KGaA, Titisee-Neustadt, Germany). Two pressure metrics were evaluated: (1) maximum gauge pressure measured within the sinus lumen during the piston forward stroke (P_{max}), and (2) maximum differential pressure (ΔP_{max}) measured between the administration nostril and sinus lumen. Pressure measurements were performed over a range of piston actuation conditions to characterize the relationship between volumetric displacement rate (dV/dt) and transient pressure generation within the sinonasal system. Since effective aerosol entry into the maxillary sinuses depends on the ability of the pulsatile delivery system to generate transient pressure conditions sufficient to overcome flow resistance across the ostial canal, characterization of pressure transmission as a function of dV/dt was performed to assess the pressure conditions associated with successful aerosol delivery and identify the minimum dV/dt thresholds required for plume entry.

For sinus lumen gauge pressure measurements, the positive pressure port of the digital manometer was connected to a pressure probe inserted into the maxillary sinus cavity through the sinus access port located on the roof of the sinus cavity, whereas the reference pressure port remained exposed to ambient atmospheric conditions (P1, Figure 1f). Maximum transient sinus pressure generated during the piston forward stroke was recorded for individual piston actuation conditions. Differential pressure measurements were performed by connecting one pressure port to the administration nostril and the second pressure port to the sinus lumen probe (P2, Figure 1f). Under these conditions, positive differential pressure values were generated during the piston forward stroke, whereas negative differential pressure values were generated during piston retraction. Differential pressure measurements were performed in the RL model by measuring pressure differences between the left administration nostril and left maxillary sinus cavity.

The piston volumetric displacement rate (dV/dt) was determined from video captures of piston motion acquired during servo actuation. Videos were analyzed using video editing software (Microsoft Clipchamp, Microsoft Corporation, Redmond, WA, USA) to determine the duration required to complete individual piston strokes (t_f). The effective volumetric displacement rate was calculated as:

$$\frac{dV}{dt} = \frac{SV}{t_f} \tag{2}$$

where SV denotes the stroke volume (50 mL) and t_f denotes the measured duration of either the forward or backward piston stroke. For individual actuation conditions, maximum transient pressure values were obtained from the digital manometer application (Testo Smart App, Testo SE & Co. KGaA, Titisee-Neustadt, Germany) and related to the corresponding measured dV/dt values.

2.6. Quantification of Retained Aerosol Mass (M_{ret})

Retained aerosol mass (M_{ret}) within the maxillary sinuses was quantified using a gravimetric cotton swab sampling technique. The same sampling methodology was applied for both water aerosol and e-vapor experiments; however, differences in post-delivery handling were implemented to account for formulation-specific aerosol behavior. For water aerosol trials, retained aerosol measurements were performed immediately following cessation of aerosol delivery. The vacuum source was shut off, the sinonasal model was disconnected from the experimental apparatus, and the transparent adhesive seal covering the sinus access port was removed prior to sampling. Immediate measurement was performed to minimize evaporation-related losses of retained water aerosols following delivery cessation and thereby better preserve the retained aerosol quantity present within the sinus cavity at the conclusion of delivery. For e-vapor trials, the vacuum source was similarly shut off following delivery cessation; however, the sinonasal model was allowed to remain undisturbed for approximately 20 min before sampling to allow suspended e-vapor aerosols remaining within the sinus lumen to settle and deposit onto the sinus walls.

Retained aerosol mass was quantified through the maxillary sinus access ports (Figure 1c) using a double-sided cotton swab. Prior to sampling, the cotton swab was weighed using a precision electronic scale (Bonvoisin, San Jose, CA, USA). The sinus walls were then systematically sampled using a standardized bottom-to-top sweeping motion to ensure consistent collection across trials. Immediately following collection, the cotton swab was reweighed, and the difference in measured mass before and after sampling was recorded as the retained aerosol mass (M_{ret}).

2.7. Sar-Gel Visualization

Sar-Gel paste (Sartomer, Arkema Inc., Exton, PA, USA), a water-sensitive indicator material that changes from white to pink upon exposure to water, was used to qualitatively visualize retained water aerosol deposition patterns within the maxillary sinus cavities. Sar-Gel testing was performed to provide visual assessment of water aerosol deposition distribution across the sinus lining, as direct visualization of deposited water aerosol films during real-time pulsatile delivery testing was challenging. Sar-Gel testing was performed using the dual-passage RL model. Prior to testing, both the left and right maxillary sinus cavities were uniformly coated with Sar-Gel using cotton swabs. A small quantity of Sar-Gel paste was applied to the swab and distributed across the sinus walls using repeated back-and-forth sweeping motions to produce a thin and uniform coating layer. The cotton swab was bent as needed to facilitate coating of superior cavity regions extending toward the ostial canal and to ensure complete and consistent coverage of the sinus lining.

Following coating preparation, pulsatile water aerosol delivery was performed under the experimental conditions described previously. Following delivery cessation, the RL model was left undisturbed for approximately 10 min to allow sufficient Sar-Gel color development and contrast generation before image acquisition. The degree of pink coloration was used as a qualitative indicator of retained water vapor . Photographic images were acquired from front, lateral, and top viewing perspectives to visualize aerosol distribution within both maxillary sinuses.

2.8. Statistical Analysis

Statistical analyses were performed using numiqo (numiqo GmbH, Graz, Austria). Quantitative data are presented as mean ± standard deviation (SD). Two-sample t-tests were performed for pairwise comparisons between experimental conditions. Violin plots were used to visualize pooled retained aerosol mass (Mret) distributions across all tested configurations for water vapor and e-vapor. The following notation was used to indicate statistical significance throughout the study: $p < 0.05$, $p < 0.01$, and $p < 0.001$. Comparisons not reaching statistical significance were denoted as ns (not significant).

3. Results

3.1. Aerosol Characterization

Figure 2 presents the particle size characterization and representative plume visualization of the generated water aerosols and e-vapor aerosols. The water aerosols exhibited a broader particle size distribution (Figure 2a) with a larger mean particle size ($\mu = 6.046$ μm) and median particle size ($D50 = 5.553$ μm) compared with the e-vapor aerosols, which exhibited a narrower distribution centered around smaller particle sizes ($\mu = 3.597$ μm; $D50 = 3.394$ μm). Percentile particle size analysis further demonstrated consistently larger characteristic particle sizes for the water aerosols across the D3-D97 range (Figure 2b). Representative plume images revealed qualitative differences in plume morphology between the two aerosol media despite both being dispensed through the same 10 mm ID silicone tube (Figures 2c&d). The water aerosol plume exhibited greater apparent gravitational settling effects, whereas the e-vapor plume appeared more concentrated and displayed a more diffuse gas-like propagation downstream of the tube outlet.

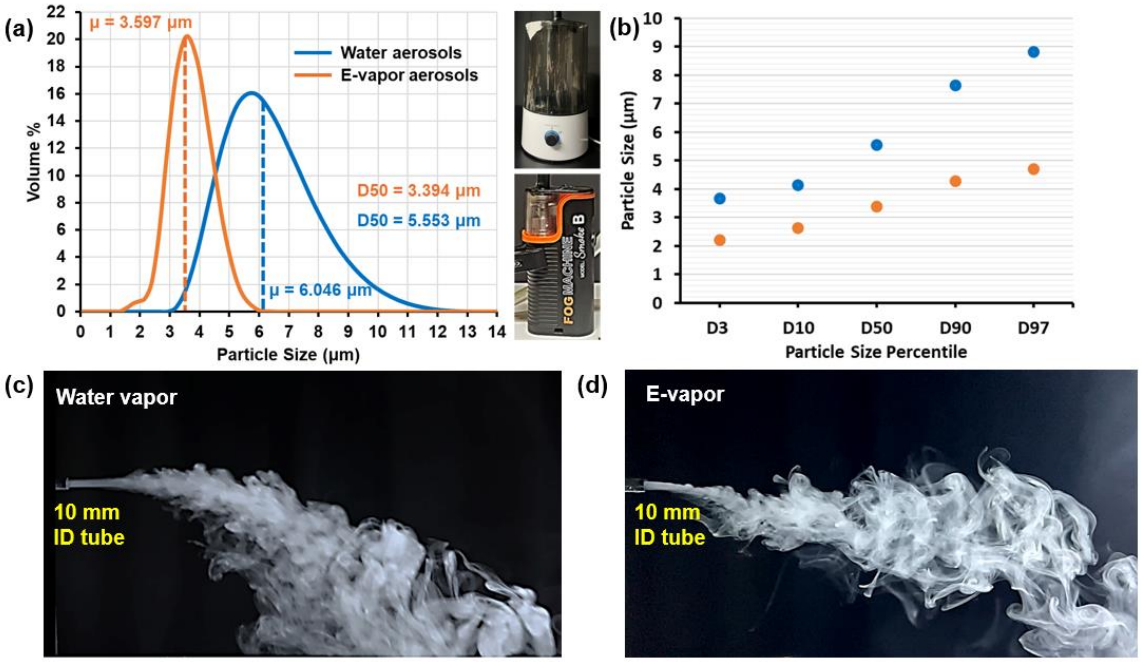

Figure 2. Aerosol characterization and representative plume visualization. (a) Particle size distributions and (b) characteristic particle size percentile plots (D3, D10, D50, D90, and D97) for water aerosols and e-vapor aerosols. Representative plume images of (c) water vapor and (d) e-vapor.

3.2. Pressure Response and Threshold Behavior

Figure 3 presents the measured maximum sinus pressures (P_{max}) as functions of dV/dt for the NL, WS, and RL sinonasal models. In all models, increasing dV/dt, which governs the intensity of pulsatile actuation, resulted in increasing measured maximum sinus pressures, indicating stronger transient pressure transmission into the maxillary sinus with increasing pulsatile actuation intensity.

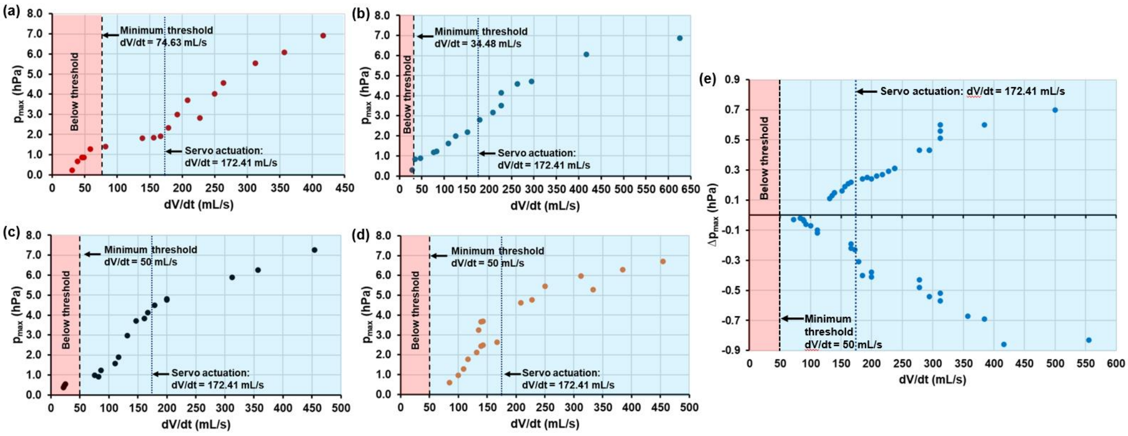

Figure 3. Maximum pressures measured in the sinonasal models as functions of dV/dt. Plots show P_{max} measured within the sinus lumen of the (a) NL, (b) WS, (c) left sinus of the dual-passage RL model, and (d) right sinus of the RL model. Measurements were obtained using a digital differential pressure manometer (Testo 510i Smart Probe) connected to the sinus lumen through the access port. Panel (e) shows ΔP_{max} measured between the nostril inlet and the left sinus lumen of the RL model as a function of dV/dt.

Distinct minimum dV/dt thresholds associated with successful plume entry into the sinus cavity were observed for the different models. The NL model exhibited the highest observed threshold (74.63 mL/s), whereas the WS model exhibited a substantially lower threshold (34.48 mL/s). The left and right maxillary sinuses of the RL model both exhibited minimum observed thresholds of approximately 50 mL/s. Below these thresholds, visible plume entry into the sinus cavity was not observed.

The servo-actuated pulsation generator used in the present study produced an effective dV/dt of 172.41 mL/s, which exceeded the minimum observed plume-entry thresholds for all tested models. Under these delivery conditions, successful plume entry into the maxillary sinuses was consistently observed in the NL, WS, and RL models. Figure 3e presents the measured maximum differential pressure (ΔP_{max}) between the nostril inlet and the left maxillary sinus lumen of the RL model as a function of dV/dt. Positive and negative ΔP_{max} values were observed corresponding to the forward and backward piston strokes, respectively. The magnitudes of both the positive and negative ΔP_{max} values generally increased with increasing dV/dt, indicating progressively stronger transient pressure differences between the nostril inlet and sinus cavity with increasing pulsatile actuation intensity. The forward- and backward-stroke ΔP_{max} trends exhibited approximately similar magnitudes and distributions across the tested dV/dt range, suggesting transient bidirectional pressure behavior during the pulsatile actuation cycle.

3.3. Spatiotemporal Plume Propagation

Representative snapshots of plume propagation within the sinonasal models are shown in Figure 4. Under pulsatile delivery, both water vapor and e-vapor plumes successfully entered the maxillary sinuses in the NL, WS, and RL models, including both the right (RL(R)) and left (RL(L)) maxillary sinuses of the dual-passage model (Figures 4a&b). Following ostial entry, the plumes generally exhibited curvilinear propagation trajectories within the sinus cavity. Among all tested configurations, the NL model, which featured the longest ostial canal, exhibited the longest apparent intraluminal plume propagation distance for both water vapor and e-vapor (Figures 4a&b, first panel pairs). Under the same delivery conditions, the plume trajectories within the RL maxillary sinuses appeared shorter than those observed in the NL and WS models (Figures 4a&b, third and fourth panel pairs). This observation may be associated with differences in sinus cavity geometry and volume between the RL and single-passage models.

Qualitative differences in intraluminal plume behavior were observed between water vapor and e-vapor. In contrast to e-vapor, where visibly suspended plumes progressively accumulated within the sinus lumen with repeated pulsations, water aerosols did not exhibit visible intraluminal buildup at the tested delivery frequency (~0.33 Hz). Instead, each delivered water-aerosol plume transiently propagated within the sinus cavity and subsequently disappeared, presumably due to wall deposition and/or rapid evaporation. The e-vapor plumes, in comparison, remained visibly suspended within the sinus lumen for longer durations and exhibited greater apparent intraluminal accumulation with successive pulsations. Supplemental Video S1 demonstrates the successful pulsatile delivery of both water vapor and e-vapor plumes under the delivery conditions used in this study.

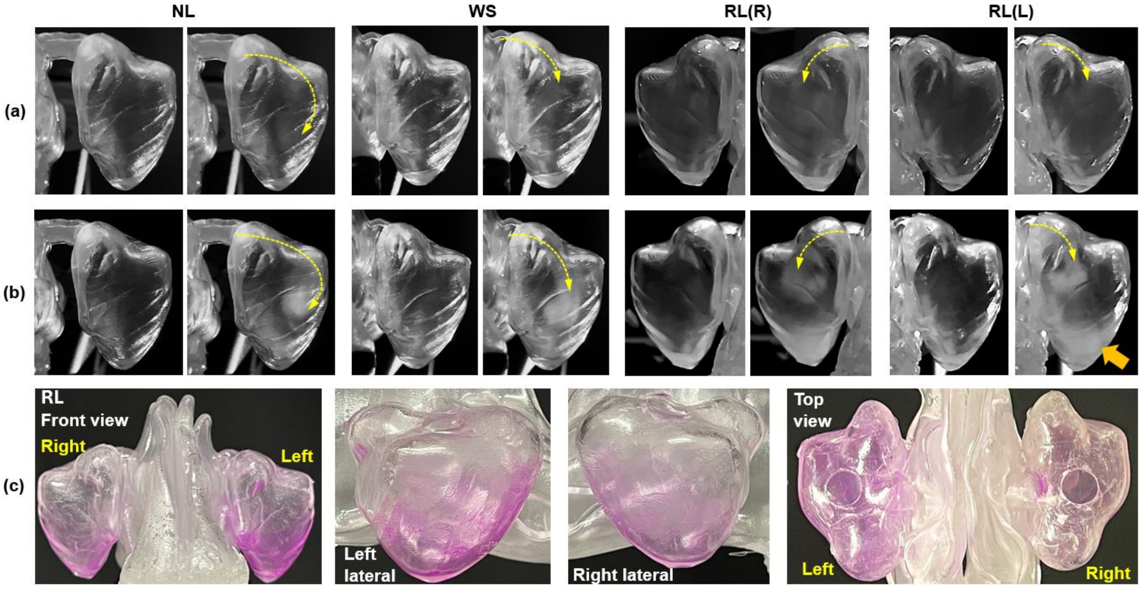

Figure 4. Representative spatiotemporal plume propagation and water aerosol retention patterns in the sinonasal models. Snapshots illustrate the trajectory of a pulsatile aerosol/vapor plume entering the maxillary sinus cavity through the ostial canal in the narrow-long (NL), wide-short (WS), and dual-passage RL models, including the right (RL(R)) and left (RL(L)) maxillary sinuses, for (a) water vapor and (b) e-vapor under pulsatile delivery. Dashed arrows indicate the general direction of plume propagation within the sinus cavity following ostial entry. (c) Sar-Gel visualization of retained water aerosols within the right and left maxillary sinuses of the RL model shown from front, lateral, and top views. Increasing pink coloration indicates greater retained water aerosol deposition.

One noteworthy phenomenon observed during pulsatile delivery was the generation of a secondary plume following the main plume. This secondary plume was observed near the beginning of the backward stroke of the piston of the pulsatile generator. Representative snapshots of both the main plume and secondary plume during e-vapor delivery within the NL and WS sinonasal models during a single pulsatile actuation cycle are shown in Figures 5a and 5b, respectively. The secondary plume appeared fainter, smaller and shorter in duration than the main plume. The main and secondary plume events occurred at two distinct time points during the pulsatile actuation cycle. Based on the threshold behavior observed in Figure 3, plume entry appears to occur once a sufficient transient pressure response is generated, rather than necessarily at the maximum sinus pressure response associated with servo actuation. These events appeared to occur when the transient local pressure conditions at the ostial opening were sufficient to overcome the transient pressure gradient and hydraulic resistance across the ostial canal, thereby allowing vapor propulsion into the sinus cavity. As observed in Supplemental Video S1, the secondary plume occurred during the early phase of the backward stroke of the piston of the pulsatile generator. The approximate timing of the main and secondary plume events relative to the pulsatile actuation cycle is illustrated schematically in Figure 5c.

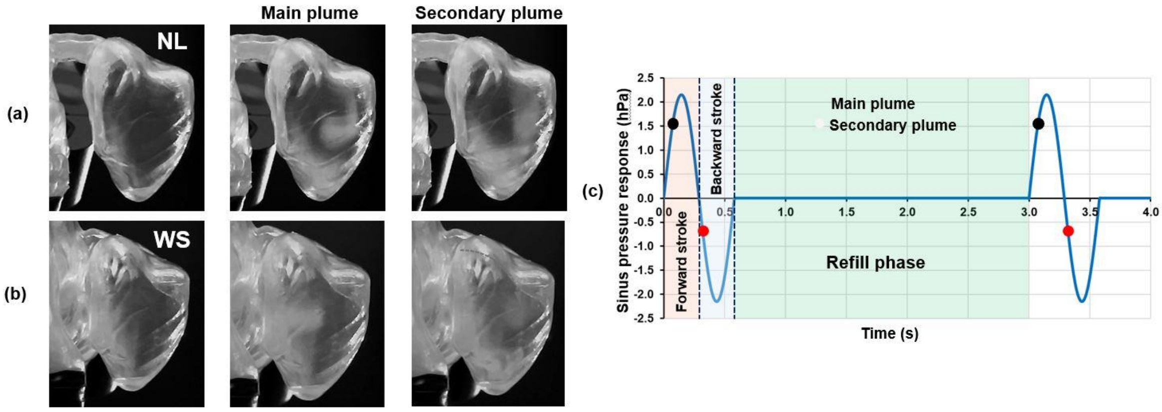

Figure 5. Observation of the "double-plume" phenomenon during pulsatile aerosol delivery. Representative snapshots showing the generation of a main plume and a secondary plume during e-vapor delivery within the (a) NL and (b) WS sinonasal models during a single pulsatile actuation cycle. The main plume was observed during the forward stroke, whereas the secondary plume was observed near the beginning of the backward stroke. (c) Schematic intermittent pulsatile pressure waveform illustrating the approximate timing of the observed plume events relative to the actuation cycle. The waveform is conceptual and based on the measured actuation timing and sinus pressure response.

3.4. Retained Aerosol Mass (M_{ret})

Figure 6 presents the retained aerosol mass (M_{ret}) for water vapor and e-vapor under identical delivery conditions. Overall, e-vapor exhibited greater M_{ret} than water vapor across all tested sinonasal configurations. In the single-passage models, the NL model exhibited mean M_{ret} values of 0.540 ± 0.089 mg for water vapor and 1.060 ± 0.152 mg for e-vapor, whereas the WS model exhibited mean M_{ret} values of 0.520 ± 0.110 mg and 0.800 ± 0.071 mg, respectively. Statistical comparison between water vapor and e-vapor demonstrated significant differences in both the NL ($p = 0.0002$) and WS ($p = 0.0014$) models. However, no significant difference in water vapor retention was observed between the NL and WS models ($p = 0.760$), whereas e-vapor retention in the NL model was significantly greater than in the WS model ($p = 0.0084$).

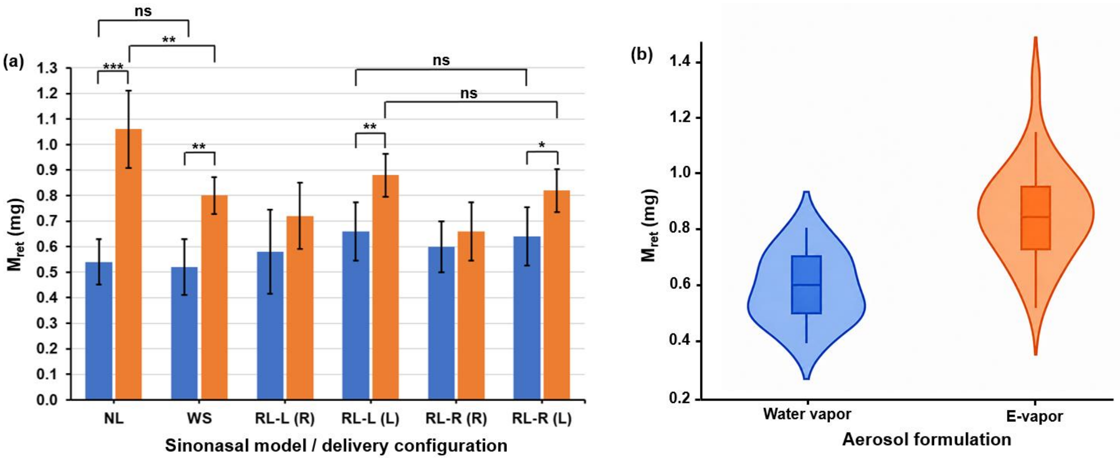

Figure 6. Retained aerosol mass (M_{ret}) outcomes for water vapor and e-vapor under pulsatile delivery conditions (SV = 50 mL, f = 0.33 Hz, Q = 1 L/min, delivery duration = 1.5 min). (a) Mean M_{ret} within the sinonasal models for water vapor and e-vapor. Results are shown for the narrow-long (NL), wide-short (WS), and dual-passage RL models, including measurements in the right (R) and left (L) maxillary sinuses following left- (RL-L) and right- (RL-R) nostril administration. Statistical comparisons were performed using two-sample t-tests. Data are summarized as mean ± SD. (b) Violin plot distributions of M_{ret} pooled across all tested configurations for water vapor and e-vapor. p-value notation: * $p < 0.05$, ** $p < 0.01$, *** $p < 0.001$; ns, not significant.

In the dual-passage RL model, bilateral aerosol delivery to both maxillary sinuses was observed regardless of the nostril of administration. Following left nostril administration, retained mass within the right and left maxillary sinuses was 0.580 ± 0.164 mg and 0.660 ± 0.114 mg, respectively, for water vapor, and 0.720 ± 0.130 mg and 0.880 ± 0.084 mg, respectively, for e-vapor. Following right nostril administration, retained mass within the right and left maxillary sinuses was 0.600 ± 0.100 mg and 0.640 ± 0.114 mg, respectively, for water vapor, and 0.660 ± 0.114 mg and 0.820 ± 0.084 mg, respectively, for e-vapor.

Statistically significant differences between water vapor and e-vapor were observed in the left maxillary sinus for both left nostril administration (RL-L(L), p = 0.0083) and right nostril administration (RL-R(L), p = 0.0216). In contrast, comparisons between left nostril and right nostril administration for retained mass within the left maxillary sinus demonstrated no significant differences for either water vapor (p = 0.789) or e-vapor (p = 0.290). The pooled violin plot distributions shown in Figure 6b further demonstrated greater overall retained aerosol mass for e-vapor relative to water vapor across all tested configurations. The water vapor distribution exhibited a lower median and narrower overall spread, whereas the e-vapor distribution was shifted toward higher retained mass values with a broader upper range extending to 1.3 mg.

3.5. Sar-Gel Retention Patterns

Representative Sar-Gel visualizations of retained water aerosols within the RL model are shown in Figure 4c. Pink coloration observed along the sinus walls indicates retained water aerosol deposition, with greater coloration intensity corresponding to greater retained aerosol accumulation. The Sar-Gel visualizations confirmed successful transport and deposition of water aerosols within both maxillary sinuses of the RL model. Retained aerosol deposition was observed from front, lateral, and top-view perspectives, demonstrating widespread sinus wall coverage following pulsatile delivery. Qualitatively, greater pink coloration intensity was observed within the left maxillary sinus compared with the right maxillary sinus, suggesting greater retained water aerosol accumulation within the left sinus cavity under the tested delivery conditions.

4. Discussion

4.1. Translation of Pulsatile Delivery from E-Vapor to Water Aerosols

The present study demonstrated that the pulsatile intra-sinus delivery approach previously developed for e-vapor aerosols could be translated to humidifier-generated water aerosols; however, substantial differences in aerosol transport behavior necessitated modifications to the delivery setup and methodology. The original pulsatile delivery system had been optimized primarily for oil-based e-vapor aerosols generated from propylene glycol/vegetable glycerin formulations [21], which exhibited transport characteristics resembling those of a quasi-gaseous medium. In contrast, humidifier-generated water aerosols displayed markedly different transport behavior throughout the delivery pathway. Compared with e-vapor aerosols, water aerosols exhibited substantially stronger surface interactions and a greater tendency toward wall deposition, condensation, and droplet coalescence within tubing and flow-control components [50,53]. These effects promoted aerosol transport losses prior to reaching the sinonasal cavity and increased sensitivity to geometric restrictions within the delivery system [54]. Components that functioned effectively during e-vapor administration, particularly one-way valve assemblies, introduced increased aerosol accumulation and transport resistance during water aerosol delivery, thereby impairing pulsatile aerosol transport efficiency [49,55]. Liquid accumulation along the inner wall further reduced aerosol available for sinus delivery.

Accordingly, modifications to the original delivery design were needed to preserve effective pulsatile transport of water vapor aerosols. Elimination of downstream one-way valves, implementation of a syringe intake port permitting chamber filling during piston retraction, and incorporation of an intermittent refill phase collectively enabled effective translation of the pulsatile delivery approach to water vapor aerosol administration. The observed formulation-dependent differences are likely attributable to fundamental differences in aerosol transport characteristics. The e-vapor aerosols propagated through the delivery system more similarly to a quasi-gaseous medium, exhibiting lower susceptibility to inertial losses, condensation, and liquid accumulation. Conversely, humidifier-generated water aerosols behaved more as discrete liquid droplets with stronger surface interactions and enhanced coalescence tendencies, rendering them considerably more sensitive to transport losses and geometric restrictions within the delivery pathway.

These findings emphasize that aerosol formulation represents an important consideration when translating pulsatile intranasal delivery technologies across aerosol platforms. Delivery systems optimized for one aerosol medium may not necessarily be directly transferable to another without design modifications that account for formulation-dependent aerosol transport behavior.

4.2. *Pressure-Driven Pulsatile Transport Mechanisms*

The present findings demonstrate that effective pulsatile aerosol transport into the maxillary sinus is fundamentally governed by the ability of the delivery system to generate transient pressure conditions sufficient to overcome hydraulic resistance across the ostial canal. Regardless of delivery system architecture, successful sinus entry ultimately depends on generating sufficiently large transient pressure disturbances capable of promoting aerosol transport across the ostial opening. Delivery system parameters including stroke volume (SV), pulsation frequency (f), tubing configuration, downstream resistance conditions, and actuation strategy influence transport primarily through their collective effects on transient pressure generation and transmission within the sinonasal system. The observed increase in measured maximum sinus pressure (P_{max}) with increasing volumetric displacement rate (dV/dt) supports this mechanism (Figure 3). Increasing dV/dt increased the intensity of pulsatile actuation and strengthened transient pressure transmission into the sinus lumen. Model-specific threshold dV/dt conditions were additionally observed, below which plume entry into the sinus cavity was not observed (Figures 3a-e, shaded red regions). The higher threshold observed in the NL model (Figure 3a) relative to the WS model (Figure 3b) is consistent with increased hydraulic resistance associated with the narrower and longer ostial canal geometry. The RL model showed intermediate thresholds, further supporting the importance of ostial geometry in governing pulsatile transport requirements.

Transient aerosol entry into the sinus appears to occur when locally generated pressure gradients become sufficient to overcome the hydraulic resistance across the ostial canal, which initiate transport into the sinus lumen. Importantly, the point of maximum measured sinus pressure did not necessarily coincide with the timing of main plume generation (Figures 3&5c). Rather, plume initiation likely occurs earlier during piston actuation when forward flow acceleration and favorable transient flow conditions develop near the ostial opening. The imposed downstream resistance established by vacuum-induced flow conditions represents an additional governing factor influencing pulsatile transport behavior. Under pulsatile delivery conditions, the sinonasal system behaves as a transiently pressurized flow domain in which externally imposed downstream resistance interacts with pulsatile pressure disturbances to facilitate aerosol entry into the sinus cavity. Downstream resistance influences transient pressure transmission throughout the sinonasal passage and therefore directly affects the ability of pulsatile disturbances to generate transport-driving pressure gradients across the ostial canal.

Once sinus entry is initiated, transient bidirectional volumetric exchange occurs across the ostial canal. Delivered aerosol entering the sinus cavity displaces resident sinus air, producing simultaneous opposing volumetric exchange while maintaining net positive aerosol transport into the sinus lumen [56,57]. This exchange process likely contributes to sustained filling behavior during delivery and may continue until transient transport equilibrium conditions are approached.

An additional phenomenon observed during pulsatile delivery was the generation of a secondary plume occurring during the early phase of piston retraction (Figures 5a-c). The secondary plume was consistently smaller, fainter, and shorter in duration than the main plume generated during the forward stroke. The mechanisms governing this secondary transport event remain incompletely understood but likely involve transient exchange dynamics and pressure redistribution within the sinonasal system during piston retraction. However, future studies were needed to elucidate the mechanisms underlying this phenomenon.

The present findings suggest that the volumetric displacement rate (dV/dt) is an important design parameter for future pulsatile delivery systems. Although the present implementation utilized a specific servo-actuated syringe architecture, the governing requirement for effective transport is not the precise configuration itself but rather the ability of the system to generate transient pressure disturbances sufficient to exceed geometry-dependent transport thresholds while maintaining physiologically acceptable transient pressure levels. Under the delivery conditions generated by the servo-actuated pulsation generator used in the present study, the maximum measured sinus pressure was 2.15 hPa (≈2.19 cmH_2O). Even at the maximum dV/dt condition assessed experimentally, the measured maximum sinus pressure remained only slightly above 7.27 hPa (≈7.41 cmH_2O) (Figure 3c), which is substantially lower than pressures commonly applied during nasal CPAP therapy (15–20 cmH_2O) [58–60], as well as below oscillatory pressure amplitudes reported for commercial pulsatile sinonasal aerosol delivery systems (~20 cmH_2O) [8].

4.3. Effects of Aerosol Formulation and Sinonasal Geometry on Transport and Retention

Both aerosol formulation and sinonasal geometry strongly influenced pulsatile transport and retention behavior within the maxillary sinuses. Overall, e-vapor aerosols generally exhibited greater retained aerosol mass (M_{ret}) compared with humidifier-generated water aerosols under identical pulsatile delivery conditions (Figure 6). The differences between the two aerosol formulations were particularly pronounced in the NL and WS models, where M_{ret} increased from 0.540 ± 0.089 mg to 1.060 ± 0.152 mg in the NL model and from 0.520 ± 0.110 mg to 0.800 ± 0.071 mg in the WS model for water aerosols and e-vapor aerosols, respectively. These differences suggest that aerosol transport and retention behavior remained highly sensitive to local ostial geometry and aerosol physicochemical characteristics.

Compared with e-vapor aerosols, humidifier-generated water vapor aerosols exhibited stronger surface interactions, enhanced coalescence tendencies, and greater susceptibility to wall deposition and evaporation losses throughout the delivery pathway and within the sinonasal cavity. These effects likely reduced the effective aerosol quantity available for sustained intraluminal transport and retention. In contrast, the e-vapor aerosols propagated more similarly to a quasi-gaseous medium and remained visibly suspended within the sinus lumen for longer durations (Figure 4b, orange arrow), thereby promoting greater apparent intraluminal accumulation and retained aerosol mass.

Sinonasal geometry additionally exerted a notable influence on retention behavior. The NL model generally exhibited greater retained aerosol mass than the WS model (Figure 6a), particularly for e-vapor aerosols (1.060 ± 0.152 mg vs. 0.800 ± 0.071 mg), despite the WS model exhibiting lower threshold conditions for plume entry (Figure 3). This suggests that effective sinus delivery is governed not only by ease of sinus entry, but also by subsequent aerosol escape dynamics and retention behavior within the sinus cavity. The narrower and longer ostial canal geometry of the NL model likely increased transport resistance during both aerosol entry and post-entry escape, thereby promoting greater aerosol retention. Conversely, the wider and shorter ostial geometry of the WS model facilitated greater sinus ventilation and aerosol washout, reducing retained aerosol mass despite more favorable entry conditions. These observations are consistent with findings from our previous in vitro study using the same NL and WS sinonasal geometries, which demonstrated that wider and shorter ostial canal configurations promoted more rapid maxillary sinus ventilation and e-vapor clearance, whereas narrower and longer ostial geometries prolonged retention and delayed transport dynamics [13].

The sinus geometrical effects were also manifested in Sar-Gel visualization of vapor deposition in the RL model. Qualitatively, greater retained water aerosol deposition was observed within the left maxillary sinus relative to the right sinus, as evidenced by the greater intensity and extent of pink Sar-Gel coloration (Figure 4c). This asymmetry is likely associated with the differences in minimum ostial cross-sectional area. As shown in Table 1, the left ostial canal featured a narrower minimum cross-sectional area than the right (11.48 mm^2 vs. 13.41 mm^2). Under the tested pulsatile delivery conditions, the narrower left ostial geometry likely reduced aerosol escape from the sinus cavity and thereby promoted greater retained aerosol accumulation.

4.4. Clinical / Device Implications

Efficient aerosol delivery into the maxillary sinuses remains difficult because the administered aerosols must penetrate relatively narrow ostial pathways before reaching the sinus cavity lumen [6,14,29]. The current results suggest that pulsatile intranasal delivery may help overcome these transport limitations by generating transient pressure-driven exchange across the ostial canal, thereby facilitating aerosol entry and retention within the sinus cavity. Such transport enhancement may prove beneficial for future localized sinonasal therapies targeting diseases involving maxillary sinuses, including chronic rhinosinusitis. The observations of this study additionally demonstrate that successful pulsatile sinus delivery depends on a combination of anatomical, aerosol, and device-related factors. While the current pulsatile delivery approach was successfully translated from e-vapor to humidifier-generated water aerosols, substantial modifications to the delivery architecture were required because of formulation-dependent differences in aerosol transport behavior. Water aerosols exhibited greater susceptibility to coalescence, wall interactions, condensation, and transport losses, indicating that future pulsatile delivery systems may require aerosol-specific design optimization depending on the formulation being administered.

The experimentally observed threshold behavior additionally suggests that future pulsatile delivery technologies should be designed to generate transient pressure disturbances sufficiently large to overcome geometry-dependent transport resistance while remaining within physiologically acceptable pressure ranges. Parameters including volumetric displacement rate (dV/dt), stroke volume, pulsation frequency, and imposed downstream resistance conditions may therefore represent important controllable variables during future device optimization. Furthermore, successful bilateral sinus delivery observed in the RL model regardless of the nostril of administration suggests that either nostril may potentially serve as an effective administration pathway during pulsatile sinonasal delivery. These observations collectively provide translational guidance for the future development of pulsatile sinonasal aerosol delivery systems and highlight the importance of simultaneously considering aerosol formulation behavior, pulsatile transport dynamics, and patient-specific sinonasal geometry during device design.

4.5. Limitations

This study has several limitations. First, the experimental investigation utilized a limited number of sinonasal models reconstructed from a single adult subject. Although the selected geometries enabled controlled investigation of ostial canal effects on pulsatile transport and retention behavior, broader patient-specific cohorts encompassing wider anatomical variability are needed for future investigations [61]. In addition, the present study focused only on the maxillary sinuses. Future work will extend the pulsatile delivery approach to anatomically complete sinonasal models incorporating the full set of paranasal sinuses to further evaluate aerosol transport behavior throughout the sinonasal system. Second, the sinonasal casts employed in this study were rigid and did not incorporate mucus layers, mucociliary clearance, or tissue compliance, all of which may influence aerosol transport, retention, and residence time under in vivo conditions [18]. The present study additionally utilized humidifier-generated water aerosols and e-vapor aerosols possessing distinct physicochemical and transport characteristics. Therapeutic aerosols or formulations with different aerodynamic properties, densities, hygroscopic behavior, or coalescence tendencies may exhibit different pulsatile transport and retention behavior and therefore require dedicated future investigation [17,62,63].

Additional limitations pertain to pressure measurements and aerosol quantification methodologies. The digital manometer used in the present study possessed limited temporal resolution and response latency, precluding precise reconstruction of the instantaneous pulsatile pressure waveform. While the instrumentation was sufficient to characterize overall pressure trends, threshold behavior, and relative transient pressure magnitudes, future studies employing higher temporal-resolution pressure measurements would permit more detailed characterization of transient transport mechanisms and plume- dynamics [64–66]. Potential evaporation-related effects might slightly underestimate the retained water aerosol mass measurements [51,67]. However, such effects were likely minimal under the present experimental conditions where measurements were rapidly made following cessation of delivery within the relatively confined maxillary sinus cavity. Importantly, quantification based solely on retained water mass might additionally underestimate the delivered dose under physiological conditions, since dissolved drug or active pharmaceutical ingredients would remain deposited on the sinonasal mucosa even after evaporation of the carrier water phase [63,68]. Furthermore, the sinonasal cavity under in vivo conditions typically exhibits very high relative humidity, which may substantially alter evaporation dynamics relative to the present in vitro experiments.

5. Conclusions

This study demonstrated the feasibility of delivering humidifier-generated water aerosols to the maxillary sinuses using low-frequency, large-amplitude pulsatile flows. Translation of the previously developed e-vapor pulsatile delivery approach to water aerosols required substantial modifications of the delivery architecture because water aerosols exhibited stronger surface interactions, greater condensation and coalescence tendencies, and increased transport losses within the delivery pathway. Elimination of downstream one-way valves, incorporation of an aerosol intake port, and use of an intermittent refill phase enabled successful pulsatile water aerosol transport under the tested conditions.

Pulsatile delivery produced successful plume entry into the maxillary sinuses of all tested sinonasal models, with minimum piston volumetric displacement-rate thresholds influenced by ostial geometry as well as broader sinonasal anatomical features that affect pressure transmission and airflow exchange. Retained aerosol mass was generally greater for e-vapor than for water aerosols under identical delivery conditions, highlighting the importance of formulation-dependent transport behavior. Sinonasal geometry also influenced delivery and retention, with narrower ostial pathways tending to promote greater retention despite higher entry resistance. Sar-Gel visualization further confirmed bilateral water aerosol delivery and retention within the dual-passage model. The findings of this study indicate that effective pulsatile sinonasal delivery depends on the combined effects of aerosol formulation, transient pressure generation, delivery-system architecture, and patient-specific sinonasal geometry. The results provide design guidance for future pulsatile intranasal delivery systems intended for water-based sinonasal therapies and support further investigation using therapeutic formulations, anatomically broader model cohorts, and more physiologically representative sinonasal conditions.

6. Patents

A U.S. provisional patent application related to this work has been filed: *Pulsatile Intranasal Delivery System for Targeted Drug Delivery to the Paranasal Sinuses*, U.S. Provisional Application No. 64/042,020, filed on April 17, 2026.

Supplementary Materials: The following supporting information can be downloaded at the website of this paper posted on Preprints.org, Video S1: Representative pulsatile delivery of water aerosols and e-vapor into NL and WS maxillary sinus models.

Author Contributions: Conceptualization, A.S., X.S. and J.X.; methodology, A.S., X.S. and J.X.; validation, A.S., X.S. and J.X.; formal analysis, A.S., X.S. and J.X.; investigation, A.S. and J.X.; resources, X.S. and J.X.; data curation, A.S. and J.X.; writing—original draft preparation, A.S.; writing—review and editing, X.S. and J. X. Visualization: A.S., X.S. and J.X.; Supervision: J.X. All authors have read and agreed to the published version of the manuscript.

Funding: This research received no external funding.

Institutional Review Board Statement: Not applicable.

Data Availability Statement: The data presented in this study are available on request from the corresponding author.

Acknowledgments: Dr. Mohamed Talaat at UMass Lowell Biomedical Engineering is gratefully acknowledged for the assistance in nasal cast preparation.

Conflicts of Interest: The authors declare no conflicts of interest.

Abbreviations

The following abbreviations are used in this manuscript:

CRS	Chronic rhinosinusitis
NL	Narrow-long ostial canal model
WS	Wide-short ostial canal model
RL	Dual-passage dual-maxillary-sinus model
RL-L	RL model with left-nostril administration
RL-R	RL model with right-nostril administration
SV	Stroke volume
Q	Vacuum-induced flow rate
M_{ret}	Retained aerosol mass
CSA	Cross-sectional area
MRI	Magnetic resonance imaging
SD	Standard deviation
ns	Not significant
CPAP	Continuous positive airway pressure

References

1. Albu, S. Chronic rhinosinusitis-an update on epidemiology, pathogenesis and management. *J. Clin. Med.* **2020**, *9*.
2. DeConde, A.S.; Soler, Z.M. Chronic rhinosinusitis: Epidemiology and burden of disease. *Am. J. Rhinol. Allergy* **2016**, *30*, 134-139.
3. Palmer, J.N.; Messina, J.C.; Biletch, R.; Grosel, K.; Mahmoud, R.A. A cross-sectional, population-based survey of U.S. adults with symptoms of chronic rhinosinusitis. *Allergy Asthma Proc.* **2019**, *40*, 48-56.
4. Bartier, S.; Coste, A.; Bequignon, E. [Management strategies for chronic rhinosinusitis with nasal polyps in adults]. *Rev. Mal. Respir.* **2021**, *38*, 183-198.

5. Medikeri, G.; Javer, A. Optimal management of allergic fungal rhinosinusitis. *J. Asthma Allergy* **2020**, *13*, 323-332.
6. Seifelnasr, A.; Zare, F.; Si, X.A.; Xi, J. Optimized gravity-driven intranasal drop administration delivers significant doses to the ostiomeatal complex and maxillary sinus. *Drug Des. Devel. Ther.* **2024**, *14*, 1839-1859.
7. Siddiqui, Z.; Tahiri, M.; Gupta, A.; Kin Nam, R.H.; Rachmanidou, A. The management of paediatric rhinosinusitis. *Int. J. Pediatr. Otorhinolaryngol.* **2021**, *147*, 110786.
8. Albu, S. Novel drug-delivery systems for patients with chronic rhinosinusitis. *Drug Des. Devel. Ther.* **2012**, *6*, 125-132.
9. Tai, J.; Lee, K.; Kim, T.H. Current Perspective on Nasal Delivery Systems for Chronic Rhinosinusitis. *Pharmaceutics* **2021**, *13*.
10. Avrunin, O.G.; Nosova, Y.V.; Abdelhamid, I.Y.; Pavlov, S.V.; Shushliapina, N.O.; Bouhlal, N.A.; Ormanbekova, A.; Iskakova, A.; Harasim, D. Research active posterior rhinomanometry tomography method for nasal breathing determining violations. *Sensors* **2021**, *21*.
11. Cankurtaran, M.; Celik, H.; Coşkun, M.; Hizal, E.; Cakmak, O. Acoustic rhinometry in healthy humans: accuracy of area estimates and ability to quantify certain anatomic structures in the nasal cavity. *Ann. Otol. Rhinol. Laryngol.* **2007**, *116*, 906-916.
12. Kwah, J.H.; Peters, A.T. Nasal polyps and rhinosinusitis. *Allergy Asthma Proc.* **2019**, *40*, 380-384.
13. Seifelnasr, A.; Si, X.A.; Xi, J. An in vitro parametric study of maxillary sinus ventilation using transparent 3D-printed sinonasal models. *Clin. Biomech.* **2026**, *133*, 106772.
14. Cheng, Y.; Holmes, T.; Gao, J.; Guilmette, R.; Li, S.; Surakitbanharn, Y.; Rowlings, C. Characterization of nasal spray pumps and deposition pattern in a replica of the human nasal airway. *J. Aerosol Med.* **2001**, *14*, 267-280.
15. Foo, M.Y.; Cheng, Y.S.; Su, W.C.; Donovan, M.D. The influence of spray properties on intranasal deposition. *J. Aerosol Med.* **2007**, *20*, 495-508.
16. Xi, J.; Yuan, J.E.; Zhang, Y.; Nevorski, D.; Wang, Z.; Zhou, Y. Visualization and quantification of nasal and olfactory deposition in a sectional adult nasal airway cast. *Pharm. Res.* **2016**, *33*, 1527-1541.
17. Guo, Y.; Tang, Y.; Su, Y.; Sun, D. Influencing factors of particle deposition in the human nasal cavity. *Laryngoscope Investig. Otolaryngol.* **2024**, *9*, e1308.
18. Seifelnasr, A.; Si, X.; Zhang, J.Y.; Luo, M.Z.; Lei, R.L.; Xi, J. Improving nasal spray deposition: advances and strategies to overcome anatomical and physiological barriers. *Expert Opin. Drug Deliv.* **2025**, *22*, 1895-1914.
19. Moeller, W.; Schuschnig, U.; Meyer, G.; Häussinger, K.; Keller, M.; Junge-Hülsing, B.; Mentzel, H. Ventilation and aerosolized drug delivery to the paranasal sinuses using pulsating airflow - a preliminary study. *Rhinology* **2009**, *47*, 405-412.
20. Möller, W.; Schuschnig, U.; Bartenstein, P.; Meyer, G.; Häussinger, K.; Schmid, O.; Becker, S. Drug delivery to paranasal sinuses using pulsating aerosols. *J. Aerosol Med. Pulm. Drug Deliv.* **2014**, *27*, 255-263.
21. Seifelnasr, A.; Si, X.A.; Xi, J. Enhanced maxillary sinus delivery using low-frequency large-amplitude pulsations in sinonasal models. *Laryngoscope* **2026**, lscope-26-1238.
22. Wofford, M.R.; Kimbell, J.S.; Frank-Ito, D.O.; Dhandha, V.; McKinney, K.A.; Fleischman, G.M.; Ebert, C.S., Jr.; Zanation, A.M.; Senior, B.A. A computational study of functional endoscopic sinus surgery and maxillary sinus drug delivery. *Rhinology* **2015**, *53*, 41-48.
23. Vahaji, S.; Shang, Y.; Zhang, Y.; Wong, E.; Rezk, A.; Yeo, L.; Vreugde, S.; Wormald, P.-J.; Singh, N.; Inthavong, K. Optimising aerosol delivery for maxillary sinus deposition in a post-FESS sinonasal cavities. *Aerosol Air Qual. Res.* **2021**, *21*, 210098.
24. Ikeda, K.; Harashima, T.; Koike, T. Effects of endoscopic sinus surgery on nasal spray deposition using dye-based methods for humans and a human silicone sinonasal cavity model. *Am. J. Otolaryngol.* **2021**, *42*, 103058.
25. Durand, M.; Le Guellec, S.; Pourchez, J.; Dubois, F.; Aubert, G.; Chantrel, G.; Vecellio, L.; Hupin, C.; De Gersem, R.; Reychler, G.; et al. Sonic aerosol therapy to target maxillary sinuses. *Eur Ann Otorhinolaryngol Head Neck Dis* **2012**, *129*, 244-250.

26. Durand, M.; Pourchez, J.; Aubert, G.; Le Guellec, S.; Navarro, L.; Forest, V.; Rusch, P.; Cottier, M. Impact of acoustic airflow nebulization on intrasinus drug deposition of a human plastinated nasal cast: new insights into the mechanisms involved. *Int. J. Pharm.* **2011**, *421*, 63-71.
27. Leclerc, L.; Merhie, A.E.; Navarro, L.; Prévôt, N.; Durand, M.; Pourchez, J. Impact of acoustic airflow on intrasinus drug deposition: New insights into the vibrating mode and the optimal acoustic frequency to enhance the delivery of nebulized antibiotic. *Int. J. Pharm.* **2015**, *494*, 227-234.
28. Leclerc, L.; Pourchez, J.; Aubert, G.; Leguellec, S.; Vecellio, L.; Cottier, M.; Durand, M. Impact of airborne particle size, acoustic airflow and breathing pattern on delivery of nebulized antibiotic into the maxillary sinuses using a realistic human nasal replica. *Pharm. Res.* **2014**, *31*, 2335-2343.
29. Möller, W.; Schuschnig, U.; Celik, G.; Münzing, W.; Bartenstein, P.; Häussinger, K.; Kreyling, W.G.; Knoch, M.; Canis, M.; Becker, S. Topical drug delivery in chronic rhinosinusitis patients before and after sinus surgery using pulsating aerosols. *PLoS One* **2013**, *8*, e74991.
30. Möller, W.; Schuschnig, U.; Khadem Saba, G.; Meyer, G.; Junge-Hülsing, B.; Keller, M.; Häussinger, K. Pulsating aerosols for drug delivery to the sinuses in healthy volunteers. *Otolaryngol. Head Neck Surg.* **2010**, *142*, 382-388.
31. Pourmehran, O.; Arjomandi, M.; Cazzolato, B.; Tian, Z.; Vreugde, S.; Javadiyan, S.; Psaltis, A.J.; Wormald, P.J. Acoustic drug delivery to the maxillary sinus. *Int. J. Pharm.* **2021**, *606*, 120927.
32. Pourmehran, O.; Zarei, K.; Pourchez, J.; Vreugde, S.; Psaltis, A.; Wormald, P.J. Advancements in acoustic drug delivery for paranasal sinuses: A comprehensive review. *Int. J. Pharm.* **2023**, *644*, 123277.
33. Xi, J.; Si, X.A.; Peters, S.; Nevorski, D.; Wen, T.; Lehman, M. Understanding the mechanisms underlying pulsating aerosol delivery to the maxillary sinus: In vitro tests and computational simulations. *Int. J. Pharm.* **2017**, *520*, 254-266.
34. Granqvist, S.; Sundberg, J.; Lundberg, J.O.; Weitzberg, E. Paranasal sinus ventilation by humming. *J. Acoust. Soc. Am.* **2006**, *119*, 2611-2617.
35. Seifelnasr, A.; Si, X.A.; Inalpolat, M.; Xi, J. Structural vibration and pulsatile flow enhance maxillary sinus ventilation: a combined experimental study and FEA modal analysis. *J. Biomech. Open* **2026**, 100006.
36. Warfield-McAlpine, P.; Fletcher, D.F.; Zhang, F.; Inthavong, K. Increasing airflow ventilation in a nasal maxillary ostium using optimised shape and pulsating flows. *Biomech. Model Mechanobiol.* **2025**, *24*, 1343-1362.
37. Weitzberg, E.; Lundberg, J.O. Humming greatly increases nasal nitric oxide. *Am. J. Respir. Crit. Care Med.* **2002**, *166*, 144-145.
38. Ghori, M.U.; Mahdi, M.H.; Smith, A.M.; Conway, B.R. Nasal drug delivery systems: an overview. *Am. J. Pharmacol. Sci.* **2015**, *3*, 110-119.
39. Keller, L.-A.; Merkel, O.; Popp, A. Intranasal drug delivery: opportunities and toxicologic challenges during drug development. *Drug Des. Devel. Ther.* **2022**, *12*, 735-757.
40. Safarov, R.; Fedotova, O.; Uvarova, A.; Gordienko, M.; Menshutina, N. Review of Intranasal Active Pharmaceutical Ingredient Delivery Systems. *Pharmaceuticals* **2024**, *17*.
41. Asgari, M.; Lucci, F.; Kuczaj, A.K. Multispecies aerosol evolution and deposition in a human respiratory tract cast model. *J. Aerosol Sci.* **2021**, *153*, 105720.
42. Kolanjiyil, A.V.; Alfaifi, A.; Aladwani, G.; Golshahi, L.; Longest, W. Importance of spray–wall interaction and post-deposition liquid motion in the transport and delivery of pharmaceutical nasal sprays. *Pharmaceutics* **2022**, *14*, 956.
43. Lin, H.; Jin, Y.; Chen, X.; Xie, J.; Lu, T.; Xu, Y. Simulating aerosol droplet dynamics and coalescence in tracheal intubation insights from a CFD-DEM analysis of PSAR tube interactions. *Powder Technol.* **2024**, *442*, 119853.
44. Zacchei, F.; Lucci, F.; Frederix, E.; Tajfirooz, S.; Kuczaj, A.K. AeroSolved: Wall boundary conditions for liquid multispecies aerosol deposition at transient and high-humidity flows. *J. Aerosol Sci.* **2025**, *188*, 106592.
45. Ariji, Y.; Kuroki, T.; Moriguchi, S.; Ariji, E.; Kanda, S. Age changes in the volume of the human maxillary sinus: a study using computed tomography. *Dentomaxillofac. Radiol.* **1994**, *23*, 163-168.
46. Dinç, K.; İçöz, D. Maxillary sinus volume changes in individuals with different craniofacial skeletal patterns: CBCT study. *BMC Oral Health* **2024**, *24*, 1516.

47. Gulec, M.; Tassoker, M.; Magat, G.; Lale, B.; Ozcan, S.; Orhan, K. Three-dimensional volumetric analysis of the maxillary sinus: a cone-beam computed tomography study. *Folia Morphol.* **2020**, *79*, 557-562.
48. Simon, E. Anatomy of the opening of the maxillary sinus. *Arch. Otolaryngol.* **1939**, *29*, 640-649.
49. Nagel, M.W.; Sadafi, H.; Suggett, J.A. Enhancing aerosol delivery in asthma and COPD: a comparison of MDI, valved holding chamber, and DPI systems using functional respiratory imaging (FRI). *Sci. Rep.* **2026**, *16*, 13148.
50. Hilpert, M.; Ilievski, V.; Hsu, S.Y.; Rule, A.M.; Olmedo, P.; Drazer, G. E-cigarette aerosol collection using converging and straight tubing Sections: Physical mechanisms. *J. Colloid Interface Sci.* **2021**, *584*, 804-815.
51. Wang, Z.; Xia, L.; Tian, L.; Wang, J.; Zhan, S.; Huo, Y.; Tu, J. Natural periodicity of electrohydrodynamic spraying in ethanol. *J. Aerosol Sci.* **2018**, *117*, 127-138.
52. Liang, L.; Lan, Y.; Yu, T.; Leng, W.; Zhang, L.; Long, Z. A comprehensive review of industrial workshop oil mist control technology based on electrostatic collection. *Atmosphere* **2025**, *16*, 242.
53. Liu, H.; Shao, J.; Jiang, W.; Liu, X. Numerical modeling of droplet aerosol coagulation, condensation/evaporation and deposition processes. *Atmosphere* **2022**, *13*, 326.
54. Wang, Z.; Li, R.; Tian, L.; Xia, L.; Zhan, S.; Wang, J.; Tu, J. Visualization of periodic emission of drops with micro-dripping mode in electrohydrodynamic (EHD) atomization. *Exp. Therm. Fluid Sci.* **2019**, *105*, 307-315.
55. Alcoforado, L.; Paiva, D.N.; Ari, A.; Barcelar, J.M.; Brandão, S.C.S.; Fink, J.B.; Dornelas de Andrade, A. Does valved holding chamber improve aerosol lung deposition with a jet nebulizer? A randomized crossover study. *Pharmaceutics* **2022**, *14*, 566.
56. Seifelnasr, A.; Si, X.; Xi, J. Experimental and computational analyses of accessory ostia effects on maxillary sinus ventilation. *J. Respir.* **2026**, *6*, 6.
57. Seifelnasr, A.; Zare, F.; Si, X.; Xi, J. Exploring e-vape aerosol penetration into paranasal sinuses: Insights from patient-specific models. *Pharmaceuticals* **2025**, *18*, 142.
58. Kushida, C.A.; Chediak, A.; Berry, R.B.; Brown, L.K.; Gozal, D.; Iber, C.; Parthasarathy, S.; Quan, S.F.; Rowley, J.A. Clinical guidelines for the manual titration of positive airway pressure in patients with obstructive sleep apnea. *J. Clin. Sleep Med.* **2008**, *4*, 157-171.
59. Lin, F.Y.; Gurgel, R.K.; Popelka, G.R.; Capasso, R. The effect of continuous positive airway pressure on middle ear pressure. *Laryngoscope* **2012**, *122*, 688-690.
60. McCormick, J.P.; Hildrew, D.M.; Lawlor, C.M.; Guittard, J.A.; Worley, N.K. Otic barotrauma resulting from continuous positive airway pressure: Case report and literature review. *Ochsner J.* **2016**, *16*, 146-149.
61. Sun, Q.; Zhang, Y.; Tian, L.; Tu, J.; Corley, R.; Kuprat, A.P.; Dong, J. Investigation of inter-subject variation in ultrafine particle deposition across human nasal airways: A study involving children, adults, and the elderly. *ci. Total Environ.* **2024**, *955*, 177028.
62. Finlay, W.H. Deposition of aerosols in the lungs: Particle characteristics. *J. Aerosol Med. Pulm. Drug Deliv.* **2021**, *34*, 213-216.
63. Wang, Z.; Tian, L.; Xia, L.; Dong, J.; Wang, J.; Tu, J. Experimental study on repetition frequency of drop/jet movement in electro-spraying of deionized water. *Aerosol Air Qual. Res.* **2018**, *18*, 301-313.
64. Li, Y.; Orr, J.; Jen, R.; Sands, S.A.; DeYoung, P.; Smales, E.; Edwards, B.; Owens, R.L.; Malhotra, A. Is there a threshold that triggers cortical arousals in obstructive sleep apnea. *Sleep* **2019**, *42*, zsz047.
65. Miechels, J.; Koning, M.V. Respiratory rate measurement by pressure variation in the high flow nasal cannula-system in healthy volunteers. *J. Clin. Monit. Comput.* **2024**, *38*, 1397-1404.
66. Patel, C.; Diba, A. Measuring tracheal airway pressures during transtracheal jet ventilation: an observational study. *Anaesthesia* **2004**, *59*, 248-251.

67. Aladwani, G.; Momin, M.A.M.; Spence, B.; Farkas, D.R.; Bonasera, S.; Hassan, A.; Hindle, M.; Longest, W. Effects of different mesh nebulizer sources on the dispersion of powder formulations produced with a new small-particle spray dryer. *Int J Pharm* **2023**, *642*, 123138.
68. Dey, S.; Tunio, M.; Boryc, L.C.; Hodgson, B.D.; Garcia, G.J.M. Quantifying strategies to minimize aerosol dispersion in dental clinics. *Exp. Comput. Multiph. Flow* **2023**, *5*, 290-303.